Fully Adaptive Multiband Bandstop Filtering Sections and Their Application to Multifunctional Components

Dimitra Psychogiou, *Member, IEEE*, Roberto Gómez-García, *Senior Member, IEEE*, and Dimitrios Peroulis, *Senior Member, IEEE*

***Abstract*— An original RF design approach for the realization of fully reconfigurable planar multiband bandstop filters (BSFs) is reported. The engineered RF filtering topology allows independent control of its stopbands in terms of center frequency and bandwidth. It exploits the in-series cascade of K spectrally agile N-notch filtering cells that are connected through $K-1$ static impedance inverters to realize an N-band filtering transfer function with Kth-order stopbands. Each of these multinotch cells is formed by N tunable resonators—center-frequency control—that interact with the same nonresonating node by means of different variable couplings—bandwidth control. Additional features of this tune-all multiband BSF architecture when compared with related prior-art devices are: 1) scalability to the synthesis of an arbitrary number of stopbands; 2) notch-spectral-merging capability into wider eliminated bands of the same order, which equivalently allows the intrinsic control, i.e., without RF switches, of the amount of active rejected bands; and 3) smaller physical size. The coupling-matrix modeling of the conceived multiband BSF scheme is presented. Moreover, its cointegration with other RF analog-processing actions in multifunctional components, such as bandpass filtering and power division, is investigated. For experimental-validation purposes, three UHF-band mechanically reconfigurable microstrip prototypes are developed and tested. They correspond to a dual-notch filter, a wideband bandpass filter with embedded notches in its tunable passband, and a Wilkinson-type power divider with inserted stopbands for dynamic multi-interference mitigation.**

***Index Terms*— Bandpass filter (BPF), bandstop filter (BSF), multiband filter, multifunctional circuit, notch filter, power divider, reconfigurable filter, tunable filter, wideband filter.**

Manuscript received July 1, 2016; revised September 9, 2016; accepted October 8, 2016. This work was developed with funding from the National Science Foundation under Award 1247893 and by the Spanish Ministry of Economy and Competitiveness under Project TEC2014-54289-R. An earlier version of this paper was presented at the IEEE MTT-S International Microwave Symposium, San Francisco, CA, USA, May 22–27, 2016.

D. Psychogiou was with the School of Electrical and Computer Engineering, Birck Nanotechnology Center, Purdue University, West Lafayette, IN 47907 USA. She is now with the Department of Electrical, Computer, and Energy Engineering, University of Colorado at Boulder, Boulder, CO 80309 USA (e-mail: dimitra.psychogiou@colorado.edu).

R. Gómez-García is with the Department of Signal Theory and Communications, Polytechnic School, University of Alcalá, 28871 Madrid, Spain (e-mail: roberto.gomez.garcia@ieee.org).

D. Peroulis is with the School of Electrical and Computer Engineering, Birck Nanotechnology Center, Purdue University, West Lafayette, IN 47907 USA (e-mail: dperouli@purdue.edu).

Color versions of one or more of the figures in this paper are available online at http://ieeexplore.ieee.org.

Digital Object Identifier 10.1109/TMTT.2016.2618396

I. Introduction

BROADBAND RF systems have recently attracted a considerable interest in high-data-rate wireless communications and ultra-wideband (UWB) radar applications [1], [2]. However, as their receiver module must acquire large portions of the electromagnetic spectrum, they can be easily desensitized by undesired out-of-system interferers that are colocated within their operational bandwidth. This is shown in Fig. 1, which shows how this plurality of simultaneously present jamming signals in the current interference-crowded environment can be effectively suppressed through a multiband bandstop filter (BSF) that is placed just before the preacquisition microwave UWB bandpass filter (BPF). Note also that, owing to the power- and frequency-agility nature of these external interferers, reconfiguration of the stopbands of the multinotch filter is highly required.

In the last few years, several examples of tune-all microwave filtering devices with multipassband-type transfer function have been proposed. Among them, some exponents to be highlighted are those based on channelized-filter-bank/double-multiplexer arrangements and multiband quasi-bandpass filtering sections with/without cross couplings [2]–[4]. Nevertheless, much less attention has been dedicated to their BSF counterparts. In relation to it, only a reduced number of discretely and continuously reconfigurable multiband BSFs have been reported. They have been developed in a variety of technologies that are based on lumped-element, hybrid-lumped-element-acoustic-wave, planar, and evanescent-mode-substrate-integrated-cavity resonators [5]–[9]. In the case of planar realizations, such as those presented in [5] and [8], they have shown some operational constraints, for example, the lack of bandwidth reconfiguration as well as control of the number of active stopbands, their limited upper passband bandwidth, and the lack of independent center-frequency reconfiguration in the filter prototype in [5]. In addition, they have been experimentally verified only in dual-stopband circuits. Moreover, due to practical aspects involved in their circuit structures, such as the use of multilayer geometries in [6] and [7] and RF transformers in [8], their real extrapolation to more-than-two-band implementations for a single stage can be more complicated than in the filtering architectures that are presented in this paper.

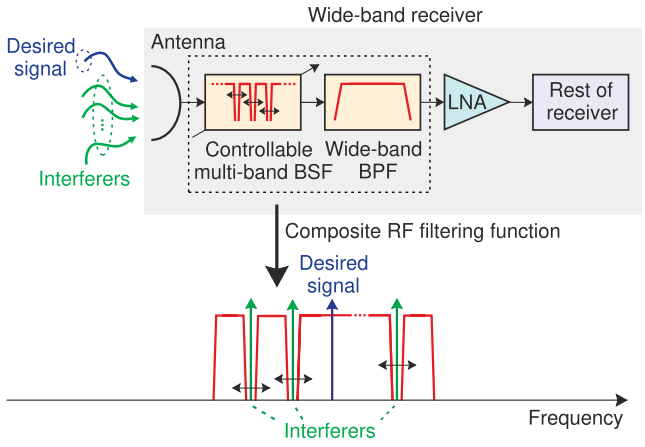

Fig. 1. Block diagram and operational principle of a wideband receiver with reconfigurable-multinotch/UWB bandpass RF filtering functionality for multi-interference mitigation (BPF: bandpass filter. BSF: bandstop filter. LNA: low-noise amplifier. UWB: ultra-wideband).

On the other hand, tunable multiband BSFs could easily be developed by simply cascading several tunable single-band bandstop filtering units as for example the ones in [10]–[14]. Nevertheless, limitations of this conventional in-series-cascade multisection approach are the larger circuit size and higher insertion-loss levels for passband ranges, as the number of interconnected bandstop filtering stages is increased.

Although the UWB bandpass and multinotch filtering units in the broadband receiver scenario represented in Fig. 1 can be synthesized separately, some combined/codesigned approaches of high-frequency filtering components that cointegrate both RF functionalities have been recently suggested. However, most of them exhibit embedded spectrally static notches [15], [16]. It should be noted that only a very few broadband BPFs with incorporated in-band tunable notches have been conceived [17]–[21]. In [17], a coplanar-waveguide UWB BPF with two spectrally agile stopbands was described. Nevertheless, it shows poor power-rejection levels and reduced tunability for its notches. Similar drawbacks are found in the double-functionality filtering topology in [18] along with its limited upper stopband attenuation. In [19] and [20], signal-interference wideband BPFs based on multipath transversal and channelized principles that create absorptive and reflective tunable in-band notches, respectively, were presented. However, especially in the BPF prototype implemented in [20], the moderate power-rejection depths of the embedded controllable stopbands are noticeably deteriorated with frequency tuning. The same performance shortcoming is shared by the UWB BPF structure suggested in [21] that is made up of variable-reactance-element-terminated cross-shaped resonators.

This paper presents a simple but efficient alternative for the design of spectrally agile planar multiband BSFs. The devised RF filter concept, which is theoretically scalable to any number of stopbands of arbitrary order, enables an independent control of its rejected bands in terms of center frequency and bandwidth. Geometrical constraints encountered when introducing all the tunable resonators, and their coupling structures needed per stage could limit its practical scalability (e.g., up to about six reconfigurable stopbands per section for a monolayer implementation with fully planar resonators, although more stopbands could be realized in alternative technologies, such as multilayer and lumped-element ones). Furthermore, as an increased spectral-flexibility level not revealed by the previous multiband BSF solutions, their eliminated bands can be dynamically combined to obtain wider rejected bands—showing the same order as the separate stopbands that are merged—and control the amount of them being active.

As novel contributions of this paper with regard to the preliminary results reported by the authors in [22], the cointegration of this tunable multiband BSF with other RF passive devices is also approached. This particularly refers to the realization of an original class of frequency-controllable broadband BPF and a Wilkinson-type power divider with embedded spectrally agile in-band notches. The engineered frequency-adaptive wideband BPF architecture, which is presented in this paper for the first time for the reported levels of spectral adaptivity, reuses the volume of the BPF circuit to incorporate multiple tunable notches in its controllable transmission band. This results in size-miniaturization and insertion-loss advantages when compared with a conventional solution based on the series cascade of separate bandpass and multinotched-band filtering units. Furthermore, unlike in the previous wideband BPF structures with in-band notches as those in [17]–[21], both the overall transmission band and the embedded rejected bands can be independently tuned in a unique RF device. Besides, as in the 3-D filter in [12] that only considers one embedded tunable stopband in its passband range, equivalent multiband bandpass filtering transfer functions with controllable center frequencies and bandwidths can be realized through this design technique. On the other hand, it should be noted that most of the prior-art dual-functionality filtering power dividers have restricted their operation to frequency-static transfer functions [23]–[27]. In relation to it, advances in the field of reconfigurable filtering power dividers have been limited to center frequency and bandwidth control of the passbands in single- and dual-band bandpass-filtering/power-distribution circuits as in [28]–[31]. Thus, to the best of our knowledge, the adaptive-multinotch/power-splitter component described in this paper can be considered among the first high-frequency devices that perform such RF-analog-processing double functionality. In addition, a more complete coupling-matrix-based formulation than in [22] and RF design guidelines are provided for the suggested filtering components.

This paper is organized as follows. In Section II, the circuit architecture and operational foundations of the proposed tune-all multiband BSF analyzed under a coupling-matrix formalism are presented. Furthermore, its co-integration with wideband BPFs and power-divider circuits to incorporate into them frequency-adaptive multi-notch filtering functionality is also expounded. As proof-of-concept demonstrators, three UHF-band reconfigurable microstrip prototypes are manufactured and characterized in Section III. They consist of a dual-band BSF, a broadband BPF that exhibits inserted notches in its controllable transmission range, and a 3-dB Wilkinson-type

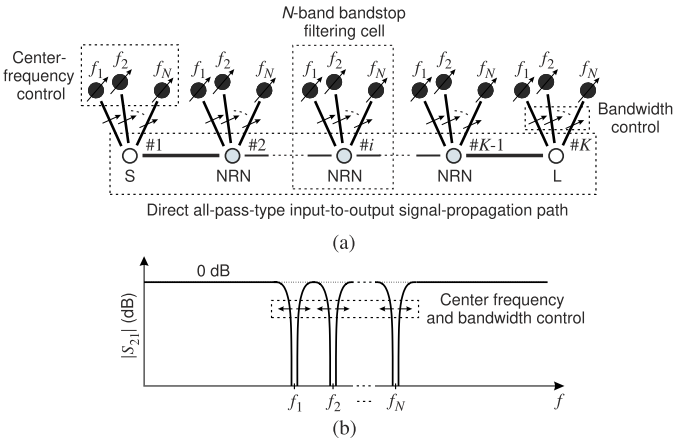

Fig. 2. Proposed fully reconfigurable multiband BSF architecture made up of K N-band bandstop filtering cells (i.e., multiband bandstop filtering transfer function with N Kth-order stopbands). (a) Coupling-matrix diagram. White circles: source (S) and load (L). Black circles: resonators. Gray circles: NRNs. Continuous lines: couplings. $f_1, f_2, \ldots, f_N$: resonant frequencies of the resonators that are equal to the center frequencies of the N generated stopbands. (b) Operating principle: the center frequencies and the bandwidths of the spectrally agile stopbands are tuned by means of the variable natural frequencies of the resonators and the controllable impedance inverters between the resonators and the NRNs, respectively.

power divider with added second-order stopbands. Finally, some concluding remarks of this paper are summarized in Section IV.

II. Theoretical Foundations

This section presents the theoretical principles of the proposed fully reconfigurable multiband BSF architecture and its extension to the realization of multiple RF analog-signal-processing functionalities at the same device. First, its conceptual scheme and operational characteristics by using a coupling-matrix formalism are illustrated. Subsequently, its cointegration with bandpass filtering networks for the synthesis of broadband BPFs with embedded in-band stopbands is approached under the same coupling-matrix framework. Finally, its application to design dual-functionality power-distribution components with embedded notches is addressed.

A. Tune-All Multiband Bandstop Filter

Fig. 2(a) shows the coupling-matrix diagram of the engineered fully reconfigurable multiband BSF configuration for the realization of a filtering response that exhibits N Kth-order stopbands. It consists of the in-series cascade of K spectrally agile N-band bandstop filtering cells by means of $K-1$ static impedance inverters that shape a direct all-pass-type input-to-output signal-propagation path. Its building adaptive N-notch filtering cell is made up of N frequency-tunable resonators that are separately coupled to the same nonresonating node (NRN) by means of variable impedance inverters. In this manner, an independent control in terms of center frequency—tunable resonators—and bandwidth—adjustable impedance inverters between the resonators and the NRN—for the N produced stopbands in the transfer function of the overall circuit is obtained. This principle of operation is shown in Fig. 2(b). Furthermore, as a benefit to be highlighted with regard to conventional multiband BSF structures based on channelized/filter-bank arrangements [32], fewer impedance

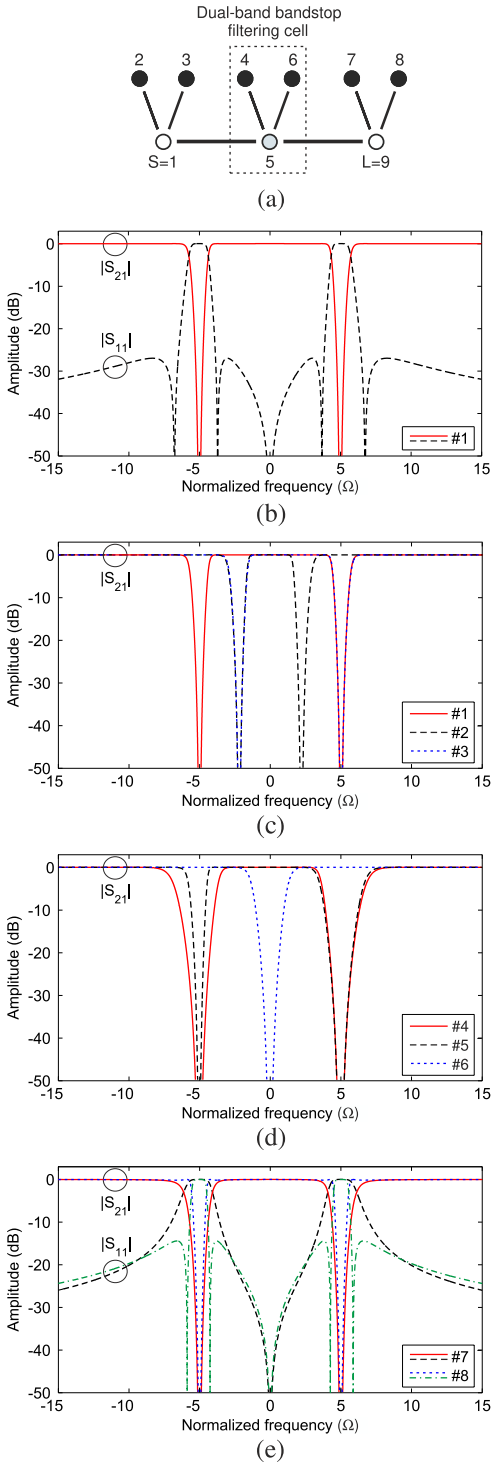

Fig. 3. Particular case of the general coupling-matrix diagram in Fig. 2(a) ($K = 3$ and $N = 2$) and examples of associated theoretical synthesized power transmission ($|S_{21}|$) and reflection ($|S_{11}|$) responses (labeled as #1, #2 . . . , #8 and having the values for the coupling-matrix coefficients in Table I). (a) Coupling-matrix diagram. (b) Example response (#1). (c) Independent center-frequency control of the stopbands (#1, #2, and #3). (d) Independent bandwidth control of the stopbands and their spectral merging (#4, #5, and #6). (e) Control of the passband input-power-matching profile and passband-to-stopband cutoff slopes (#7 and #8).

TABLE I
VALUES OF THE COUPLING-MATRIX COEFFICIENTS IN (1) FOR THE SYNTHESIZED EXAMPLES IN FIG. 3

	#1	#2	#3	#4	#5	#6	#7	#8
$M_{22} = M_{44} = M_{77}$	-5	-2.2	-5	-5	-5	0	-5	-5
$M_{33} = M_{66} = M_{88}$	5	2.2	2.2	5	5	0	5	5
$M_{12} = M_{45} = M_{79}$	0.9	0.9	0.9	1.4	1.4	0.9	0.9	0.9
$M_{13} = M_{56} = M_{89}$	0.9	0.9	0.9	1.4	0.9	0.9	0.9	0.9
$M_{15} = M_{59}$	0.8	0.8	0.8	0.8	0.8	0.8	0.6	1

inverters are required in the current approach. Note that when synthesizing a transfer function with N Kth-order stopbands, $K(N+1)-1$ impedance inverters are needed in the proposed multiband BSF solution. However, $N(2K+1)$ impedance inverters are necessary in the traditional channelized architecture. This results in insertion-loss and size-miniaturization advantages in a practical realization.

In order to theoretically validate the described operational characteristics for the devised spectrally dynamic multiband BSF approach, a specific example based on three in-series-cascaded two-notch bandstop filtering cells, i.e., transfer function with two third-order stopbands, is considered here. Its coupling-matrix diagram, which is a particularization of the general one provided in Fig. 2(a) for the case $K = 3$ and $N = 2$, is shown in Fig. 3(a). Taking into account the numbering of nodes indicated in Fig. 3(a), a coupling matrix **[M]** that models this multiband BSF scheme is given in (1). For illustration purposes, a variety of dual-band bandstop filtering transfer functions synthesized by means of (1) are plotted in Fig. 3(b)–(e). The values of the coupling-matrix coefficients associated with these responses are listed in Table I. Fig. 3(b) shows an example response—power transmission and reflection parameters—for this filter, in which the equiripple-type profile in the passband region is appreciated. Fig. 3(c) shows the independent center-frequency control for the rejected bands, whereas Fig. 3(d) demonstrates independently tunable stopbands with reconfigurable bandwidth. In Fig. 3(d), the spectral merging of the individual stopbands into a broader one of the same order, i.e., the two stopbands are combined into a unique third-order wider stopband, that is centered at the normalized frequency $\Omega = 0$ is also proved. Note that this feature allows to control the amount of stopbands that are produced in the overall transfer function independently of the number of employed resonators in its constituent multinotch filtering cell. Furthermore, it should be remarked upon that the merging of the two stopbands in this filter approach—as well as in those presented in Sections II-B and II-C—does not result into a higher order for the combined wider rejected band. This is due to the fact that the two resonators in each dual-band bandstop filtering section appear effectively connected in an in-parallel-type arrangement without an equivalent impedance inverter between them. Thus, the combination of their resonances does not lead to an increase of the order of the shaped broader stopband, unlike for resonators corresponding to different dual-band bandstop filtering sections. Finally, Fig. 3(e) verifies how the input-power-matching profile in the passband region and the passband-to-stopband cutoff slopes can be adjusted through the impedance inverters between the NRNs that shape the direct input-to-output electrical path. All these reconfiguration capabilities can be implemented in practice by introducing variable capacitors into the filter resonators as well as their corresponding couplings with the NRNs, as it will be demonstrated through the three experimental proof-of-concept prototypes that are developed and tested in Section III

$$\mathbf{M}=\begin{pmatrix} 0 & M_{12} & M_{13} & 0 & M_{15} & 0 & 0 & 0 & 0 \\ M_{12} & M_{22} & 0 & 0 & 0 & 0 & 0 & 0 & 0 \\ M_{13} & 0 & M_{33} & 0 & 0 & 0 & 0 & 0 & 0 \\ 0 & 0 & 0 & M_{44} & M_{45} & 0 & 0 & 0 & 0 \\ M_{15} & 0 & 0 & M_{45} & 0 & M_{56} & 0 & 0 & M_{59} \\ 0 & 0 & 0 & 0 & M_{56} & M_{66} & 0 & 0 & 0 \\ 0 & 0 & 0 & 0 & 0 & 0 & M_{77} & 0 & M_{79} \\ 0 & 0 & 0 & 0 & 0 & 0 & 0 & M_{88} & M_{89} \\ 0 & 0 & 0 & 0 & M_{59} & 0 & M_{79} & M_{89} & 0 \end{pmatrix}. \tag{1}$$

It should be further remarked that the multiband BSF coupling-node diagram in Fig. 2(a) and its synthesized transfer function can be obtained from an associated equivalent low-pass-type prototype by applying the following low-pass-to-multibandstop frequency transformation $\Omega^{\mathrm{MBS}}(f)$:

$$\Omega^{\mathrm{MBS}}(f) = -\sum_{i=1}^{N} \frac{1}{\frac{1}{\Delta_i}\left(\frac{f}{f_i}-\frac{f_i}{f}\right)} \tag{2}$$

where Ω is the normalized low-pass frequency, f is the bandpass frequency, f_i is the center frequency of the ith stopband, and Δ_i is a parameter that is related with the relative-to-f_i bandwidth of the ith stopband ($i = 1, 2, \ldots, N$). The Ω-to-f frequency mapping associated with this frequency transformation $\Omega^{\mathrm{MBS}}(f)$ is shown in Fig. 4 for a fourth-order two-band BSF example, i.e., $K = 4$ and $N = 2$, with the following values for the design variables in (2): $f_1 = 1$ GHz, $f_2 = 1.5$ GHz, $\Delta_1 = 0.1$, and $\Delta_2 = 2/15$.

B. Bandpass Filter With Tunable In-Band Stopbands

The tune-all multiband BSF concept expounded in Section II-A can be applied to the design of broadband BPFs with embedded spectrally agile in-band notches. This can be done by directly replacing the NRN of its constituent multiband bandstop filtering cell by a resonating node. Thus, the coupling-matrix diagram shown in Fig. 2(a) is transformed into the one shown in Fig. 5(a), in which a bandpass-filtering-type input-to-output signal-propagation path instead of an all-pass-type one is realized. The different notches associated with the multiband bandstop filtering cells are then created within the passband range of the transfer function inherent to this bandpass-type input-to-output electrical path. These embedded notches can be reconfigured in terms of center frequency and bandwidth within the transmission band of the overall BPF in a similar manner, as described in Section II-A. Moreover, when compared with a conventional series cascade of a BPF and a multinotch filtering unit to realize the same transfer function, an advantage in terms of fewer

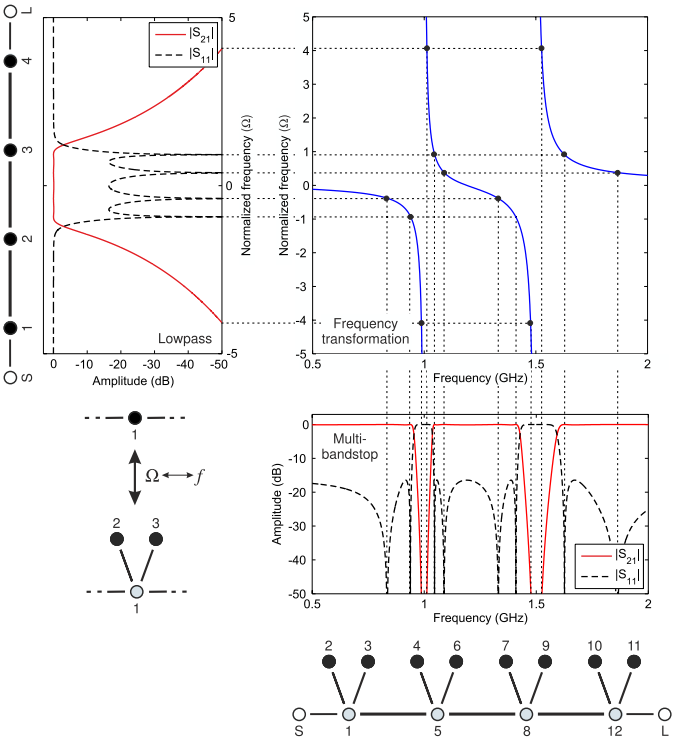

Fig. 4. Representation of the low-pass-to-multibandstop frequency transformation $\Omega^{\mathrm{MBS}}(f)$ in (2), i.e., Ω-to-f frequency mapping: example with $K = 4$, $N = 2$, $f_1 = 1$ GHz, $f_2 = 1.5$ GHz, $\Delta_1 = 0.1$, and $\Delta_2 = 2/15$.

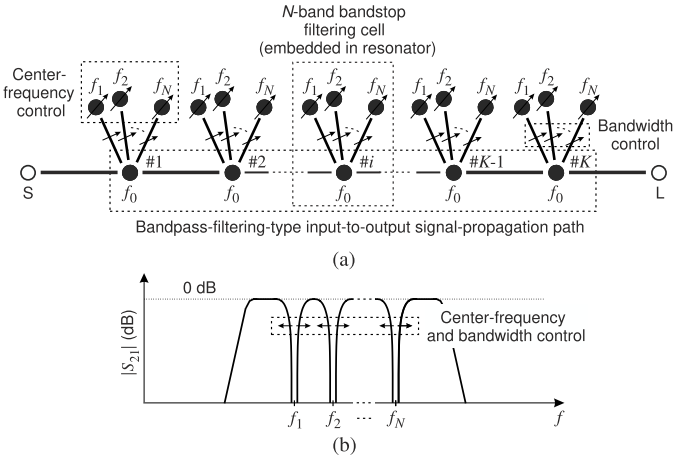

Fig. 5. Proposed wideband BPF architecture with embedded fully reconfigurable in-band notches made up of K N-band bandstop filtering cells embedded in resonators (i.e., Kth-order bandpass filtering response with N Kth-order stopbands). (a) Coupling-matrix diagram. White circles: source (S) and load (L). Black circles: resonators. Continuous lines: couplings. f_0: resonant frequency of the resonators in the input-to-output bandpass-type electrical path that is equal to the center frequency of the overall BPF. $f_1, f_2, \ldots, f_N$: resonant frequencies of the resonators that are equal to the center frequencies of the N generated in-band stopbands. (b) Operating principle: the center frequencies of the spectrally agile stopbands are tuned within the overall BPF passband by means of the variable natural frequencies of the resonators outside the input-to-output bandpass-type electrical path; their bandwidths are reconfigured with the controllable impedance inverters between these external resonators and those shaping the referred bandpass-type signal-propagation path, respectively.

impedance inverters is obtained with the current solution. Note that if the Kth-order bandpass filtering response with N in-band Kth-order stopbands is considered, the number of impedance inverters required by each alternative is as follows: $NK + K + 1$—current approach, $NK + 2K$—separate BPF and multiband BSF as the one in Fig. 2, and $N(2K + 1) + K + 1$—separate BPF and multiband BSF based on a classic channelized/filter-bank scheme (the cascading line between separate filtering units is not accounted in the cascade solutions as the adequate number of inverters to model it depends on the order of the filtering stages). Thus, fewer impedance inverters are necessary in the devised BPF/in-band-multi-BSF concept.

A specific example of the general coupling-matrix diagram detailed in Fig. 5(a) for the case $K = N = 2$, i.e., two-pole BPF with two in-band second-order notches, is provided in Fig. 6(a) along with node-numbering designation. A coupling matrix **[M]** corresponding to this BPF scheme with embedded in-band stopbands is formulated in (3). Several filtering responses synthesized through this circuit network are shown in Fig. 6(b)–(e) to theoretically illustrate its design flexibility. The values of the coupling-matrix coefficients corresponding to these filtering responses are enumerated in Table II. First, Fig. 6(b) shows an example bandpass response that exhibits two in-band notches with theoretically infinite attenuation. Independent center-frequency and bandwidth control for the two in-band rejected bands, in addition to its spectral merging, are, respectively, proved in Fig. 6(c) and (d). Note that whereas the center-frequency tuning of the stopbands does not have influence on the overall BPF passband, their bandwidth control affects the characteristics of the whole transmission band. As in Fig. 6(d), this can be counteracted by readjusting the coupling-coefficient values associated with the input-to-output bandpass-type path—symmetrical bandwidth tuning—and the natural frequencies of its resonating nodes—asymmetrical bandwidth tuning. Finally, Fig. 6(e) shows an example triple-passband filtering response with second-order equiripple-type transmission bands of comparable bandwidths. Like in other multiband BPF arrangements as the one in [33] that can also be modeled with this coupling-matrix formalism, the feasible maximum spectral separation between the lower and upper passbands is limited here by the bandwidth of the BPF associated with the input-to-output bandpass-type electrical path

$$\mathbf{M} = \begin{pmatrix} 0 & M_{12} & 0 & 0 & 0 & 0 & 0 & 0 \\ M_{12} & M_{22} & M_{23} & M_{24} & 0 & 0 & M_{27} & 0 \\ 0 & M_{23} & M_{33} & 0 & 0 & 0 & 0 & 0 \\ 0 & M_{24} & 0 & M_{44} & 0 & 0 & 0 & 0 \\ 0 & 0 & 0 & 0 & M_{55} & 0 & M_{57} & 0 \\ 0 & 0 & 0 & 0 & 0 & M_{66} & M_{67} & 0 \\ 0 & M_{27} & 0 & 0 & M_{57} & M_{67} & M_{77} & M_{78} \\ 0 & 0 & 0 & 0 & 0 & 0 & M_{78} & 0 \end{pmatrix}. \quad (3)$$

Note finally that the coupling-node diagram in Fig. 5(a) for the devised BPF concept with in-band notches and its corresponding transfer function can be derived from an associated equivalent low-pass-type prototype after applying the low-pass-to-bandpass/multibandstop frequency transformation that is detailed in the following:

$$\Omega^{\mathrm{BMB}}(f) = \frac{1}{\Delta_0}\left(\frac{f}{f_0} - \frac{f_0}{f}\right) - \sum_{i=1}^{N} \frac{1}{\frac{1}{\Delta_i}\left(\frac{f}{f_i} - \frac{f_i}{f}\right)} \quad (4)$$

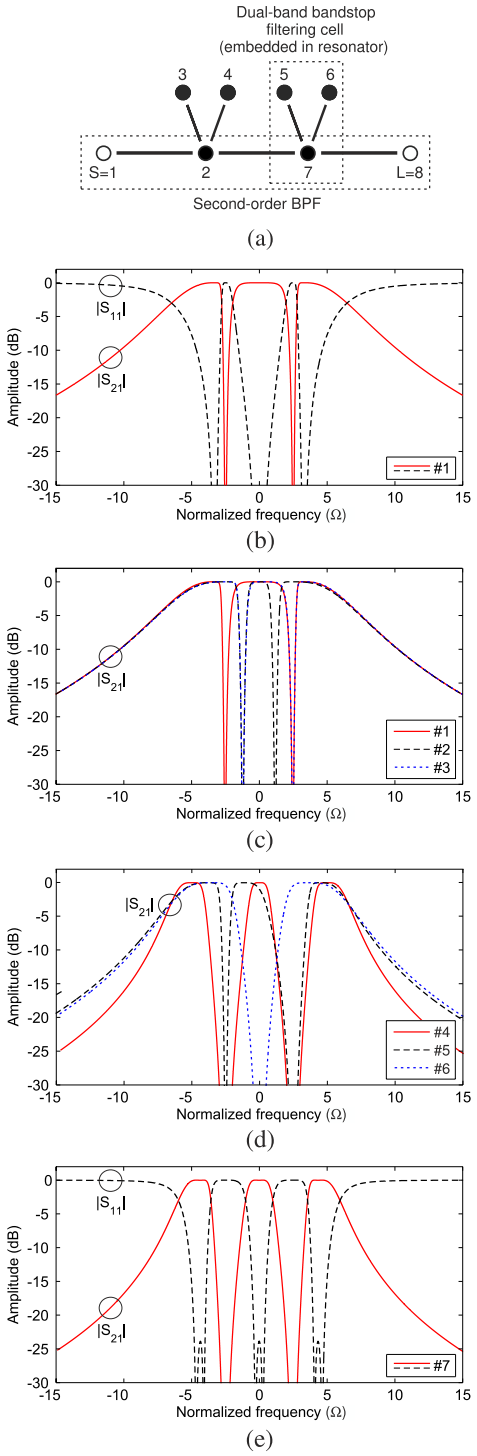

Fig. 6. Particular case of the general coupling-matrix diagram in Fig. 5(a) ($K = 2$ and $N = 2$) and examples of associated theoretical synthesized power transmission ($|S_{21}|$) and reflection ($|S_{11}|$) responses (labeled as #1, #2 . . . , #7 and having the values for the coupling-matrix coefficients in Table II). (a) Coupling-matrix diagram. (b) Example response (#1). (c) Independent center-frequency control of the stopbands (#1, #2, and #3). (d) Independent bandwidth control of the stopbands and their spectral merging (#4, #5, and #6). (e) Example of equiripple-type triple-passband response (#7).

where Ω is the normalized low-pass frequency, f is the bandpass frequency, f_0 and Δ_0 are the parameters related with the center frequency and relative-to-f_0 bandwidth of the overall transmission band, and f_i and Δ_i refer to the center

TABLE II

VALUES OF THE COUPLING-MATRIX COEFFICIENTS IN (3) FOR THE SYNTHESIZED EXAMPLES IN FIG. 6

	#1	#2	#3	#4	#5	#6	#7
$M_{33} = M_{55}$	-2.5	-1.2	-2.5	-2.5	-2.5	0	-2.5
$M_{44} = M_{66}$	2.5	1.2	1.2	2.5	2.5	0	2.5
$M_{22} = M_{77}$	0	0	0	0	0.5	0	0
$M_{23} = M_{57}$	1.5	1.5	1.5	3	3	2.5	2.5
$M_{24} = M_{67}$	1.5	1.5	1.5	3	1.5	2.5	2.5
$M_{12} = M_{78}$	2	2	2	1.5	1.8	1.8	1.5
M_{27}	4	4	4	2.3	3.2	3.2	2.4

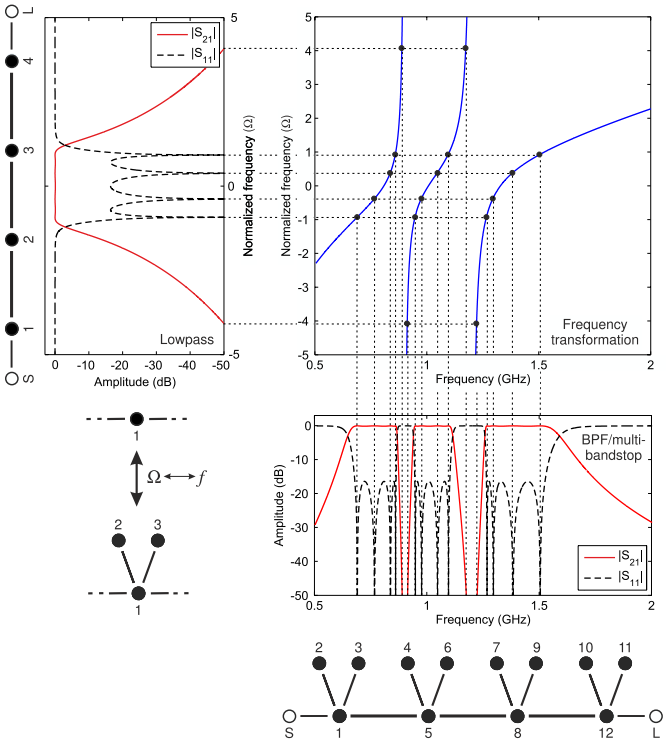

Fig. 7. Representation of the low-pass-to-bandpass/multibandstop frequency transformation $\Omega^{\mathrm{BMN}}(f)$ in (4), i.e., Ω-to-f frequency mapping: example with $K = 4$, $N = 2$, $f_0 = 1$ GHz, $f_1 = 0.9$ GHz, $f_2 = 1.2$ GHz, $\Delta_0 = 0.6$, $\Delta_1 = 1/9$, and $\Delta_2 = 1/6$.

frequency and to a variable associated with the relative-to-f_i bandwidth of the ith in-band stopband, respectively ($i = 1, 2, \ldots, N$). The Ω-to-f frequency mapping corresponding to this frequency transformation $\Omega^{\mathrm{BMB}}(f)$ is shown in Fig. 7 for a fourth-order BPF example with two embedded fourth-order rejected bands, i.e., $K = 4$ and $N = 2$, with the following values for the design parameters in (4): $f_0 = 1$ GHz, $f_1 = 0.9$ GHz, $f_2 = 1.2$ GHz, $\Delta_0 = 0.6$, $\Delta_1 = 1/9$, and $\Delta_2 = 1/6$.

C. Wilkinson Power Divider With Embedded Tunable Notches

By adopting an analogous RF design philosophy to the one presented in Section II-B, the suggested fully adaptive multi-band bandstop filtering cell can be cointegrated with other microwave passive devices to add tunable multinotch filtering

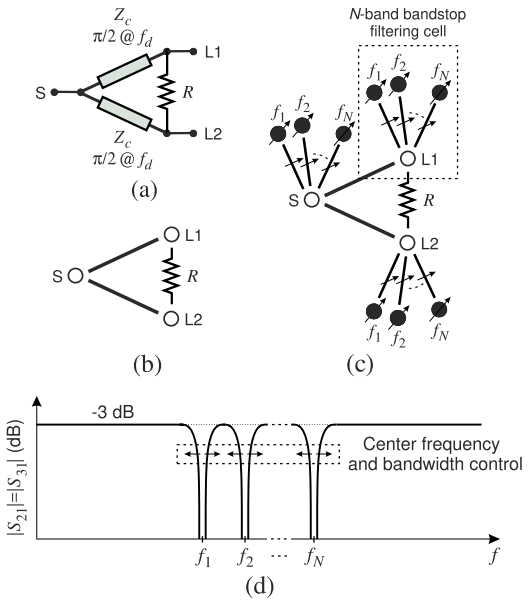

Fig. 8. Proposed 3-dB Wilkinson-type power-divider architecture with embedded fully reconfigurable in-band notches made up of three N-band bandstop filtering cells (i.e., 3-dB power-splitting action with N second-order stopbands). (a) Circuit detail of the classic 3-dB power divider ($Z_c = Z_0\sqrt{2}$ and $R = 2Z_0$). (b) Equivalent coupling-matrix diagram of the classic 3-dB power divider. White circles: source (S) and loads ($L1$ and $L2$). Gray circles: NRNs. Continuous lines: couplings. $f_1, f_2, \ldots, f_N$: resonant frequencies of the resonators that are equal to the center frequencies of the N generated stopbands. (c) Coupling-matrix diagram of the proposed 3-dB multi-BSF/power-divider circuit. (d) Operating principle: the center frequencies and the bandwidths of the spectrally agile stopbands are tuned by means of the variable natural frequencies of the resonators and the controllable impedance inverters between the resonators and the NRNs, respectively.

capabilities. Such a design is discussed in this section for the application of a Wilkinson-type single-stage/two-way power divider. Nevertheless, it is also valid for multistage designs aimed at wider band power-divider realizations. Moreover, it can be extrapolated to other families of high-frequency components, such as directional couplers and matching networks.

The proposed concept of the dual-functionality Wilkinson-type power divider with incorporated tunable multinotch filtering operation is shown in Fig. 8. Specifically, Fig. 8(a) shows the circuit scheme of the traditional two-way 3-dB Wilkinson-type power divider (i.e., $Z_c = Z_0\sqrt{2}$ and $R = 2Z_0$, where Z_0 is the reference impedance and f_d is the design frequency of the power divider). Its equivalent coupling-matrix diagram is provided in Fig. 8(b), in which the transmission-line segments of the power-divider branches can be viewed as impedance inverters at f_d and the interconnection points as NRNs. These NRNs are replaced in Fig. 8(c) by spectrally agile multiband bandstop filtering cells after following a similar RF design strategy as the one in the previous section. Thus, as shown in Fig. 8(d), tune-all second-order stopbands are added to the power-divider transfer functions between its input and the output terminals. Note that, in this approach, the transmission-line segments of the power-divider arms are reused by the power-splitting and multinotch filtering functionalities. Furthermore, the multiband bandstop filtering cell at the input node is shared by the filtering functions of both branches. Thus, less circuit size and reduced insertion loss when compared with a classic solution of a power divider with external in-series-cascaded tune-all second-order multiband BSF units at its outputs is obtained in the devised filtering power splitter. Note that, even without considering the cascading lines between separate units in the conventional approach and for the same type of N-band BSF (Fig. 2), $N - 2$ less inverters are needed in the current solution for N-stopband designs. Such benefit is even higher in multistage architectures for broader band power-divider configurations.

A particular topology of the engineered multi-BSF/power-divider device for dual-notch filtering cells, i.e., $N = 2$, is shown in Fig. 9(a). As shown, half-wavelength open-ended transmission-line resonators at the frequencies f_1 and f_2 and of characteristic impedance Z_r are used in its dual-notch filtering cells. The impedance inverters between these resonators and its adjacent NRN are realized as quarter-wavelength transmission-line segments at the frequencies f_1 and f_2 with characteristic impedances $Z_{\text{inv}1}$ and $Z_{\text{inv}2}$, respectively. Note that the values of the characteristic impedances of the line segments of the power-divider arms are not affected by the reactive effect associated with the tunable resonators and their coupling structures that are included to generate the embedded notches. As a result, a two-step procedure can be followed for the design of this multifunctional microwave component as follows: 1) synthesis of the power divider through classic techniques to obtain the required power-division factor and operational bandwidth around its design frequency (i.e., multistage arrangements, as in [34], can be considered for broad bandwidth designs) and 2) subsequent incorporation of the tunable resonators and their coupling networks into the power-divider branches to add the tunable embedded notches to their associated transfer functions. The S-parameters—in amplitude—of an example response synthesized through this specific design are shown in Fig. 9(b), in which power-matching and isolation levels higher than 10 dB throughout the full plotted passband range and two stopbands that exhibit ideally infinite attenuation are attained. The reconfiguration capabilities of this filtering power-divider example are demonstrated in Fig. 9(c) and (d) through several synthesized transfer functions, whose design parameters are summarized in Table III. Independent center-frequency tuning of the rejected bands by varying the natural frequencies of the resonators is proved in Fig. 9(c). Furthermore, separate bandwidth control for these stopbands is demonstrated in Fig. 9(d) by adjusting the line impedances of their inverters, along with its spectral merging into a single and broader rejected band. In all cases, comparable power matching and isolation performances as in the response in Fig. 9(b) are achieved.

III. Experimental Results

To practically validate the three multifunctional device concepts that were presented in Section II, various UHF-band mechanically reconfigurable microstrip prototypes referred to an impedance level $Z_0 = 50\ \Omega$ have been developed. Their design and modeling were carried out by making use of the commercial package Keysight Advanced Design System software, whereas their measurements have been performed with

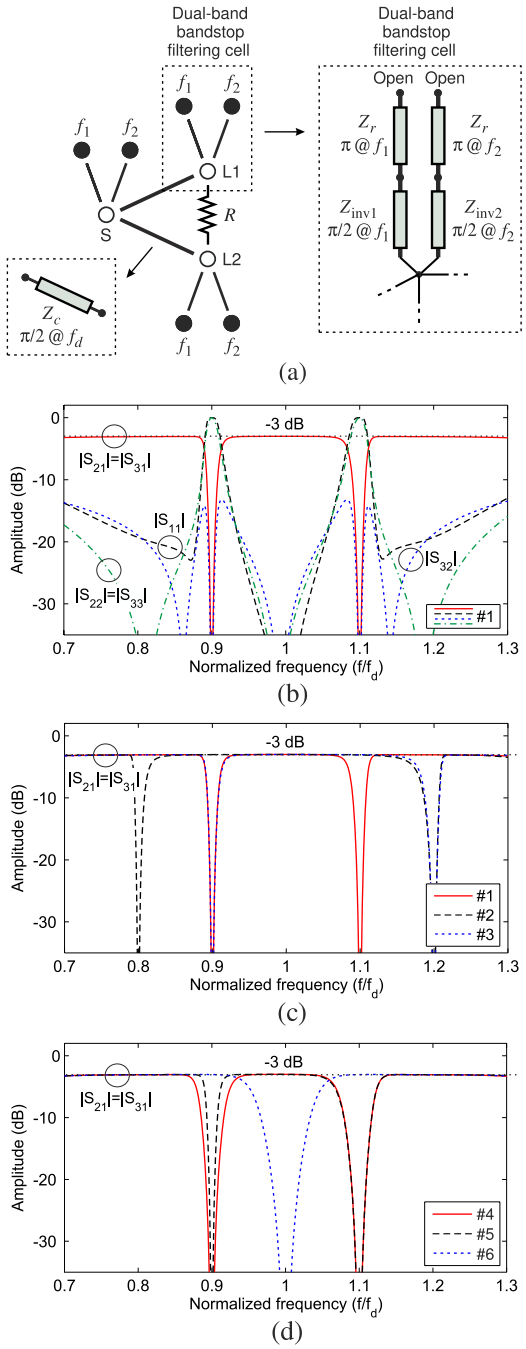

Fig. 9. Particular topology of the general multi-BSF/power-divider scheme in Fig. 8(c) ($N = 2$) and examples of associated theoretical synthesized S-parameters in amplitude (labeled as #1, #2 . . . , #6 and having the values for the design variables in Table III). (a) Circuit scheme. (b) Example response (#1). (c) Independent center-frequency control of the stopbands (#1, #2, and #3). (d) Independent bandwidth control of the stopbands and their spectral merging (#4, #5, and #6).

an Agilent-E8361A network analyzer. The results obtained in the simulation and characterization processes of these circuits are shown in the following.

A. Prototype 1

The first design example corresponds to a tune-all three-band BSF prototype with second-order eliminated bands. This

TABLE III

VALUES OF THE DESIGN PARAMETERS FOR THE SYNTHESIZED EXAMPLES IN FIG. 9

	#1	#2	#3	#4	#5	#6
f_1/f_0	0.9	0.8	0.9	0.9	0.9	1
f_2/f_0	1.1	1.2	1.2	1.1	1.1	1
Z_{inv1}/Z_0	3	3	3	2	2	2
Z_{inv2}/Z_0	3	3	3	2	3	2

(*) $Z_c = Z_0\sqrt{2}$, $R = 2Z_0$, and $Z_r = Z_0/2$ in all cases.

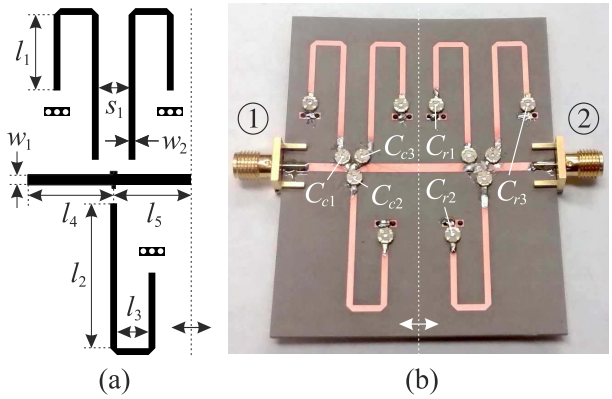

Fig. 10. Manufactured three-band second-order BSF prototype. (a) Layout (half part of the physically symmetrical schematic). Illustrated dimensions (in mm): $w_1 = 1.79$, $w_2 = 1.19$, $l_1 = 13.19$, $l_2 = 25.28$, $l_3 = 5.5$, $l_4 = 15$, $l_5 = 13.56$, and $s_1 = 5.21$. (b) Photograph.

filtering device was synthesized, so that its three rejected bands can be independently controlled in terms of center frequency and bandwidth throughout the spectral range 0.8–1.2 GHz.

The layout and a photograph of the manufactured prototype are shown in Fig. 10. If needed, further miniaturization could be achieved by meandering the transmission-line segment that connects the two triple-band bandstop filtering sections or by potential applying recently proposed short-through-line techniques to this circuit, as reported in [35] and [36], for frequency-static single-band BSFs. In both cases, the maximum feasible size-reduction level could be limited by the appearance of undesired cross-coupling effects between the physically adjacent tunable resonators embedded in different triple-band bandstop filtering stages. For the fabrication of the prototype in Fig. 10, a Rogers RT/Duroid 6006 microstrip substrate with the following parameters was employed: relative dielectric permittivity $\varepsilon_r = 6.45$, dielectric thickness $H = 1.27$ mm, metal thickness $t = 35$ μm, and dielectric loss tangent $\tan\delta_D = 0.0027$. As can be seen in Fig. 10, its tunable resonators were implemented by means of uniform-impedance transmission-line segments that are loaded with short-circuit-ended adjustable capacitors. The frequency-static impedance inverters that cascade in series the two three-band bandstop filtering cells were realized through variable capacitors that allow to incorporate bandwidth agility into the rejected bands. For the controllable capacitors of the tunable resonators and their reconfigurable couplings with the NRNs, mechanically adjustable thin-trim trimmer capacitors

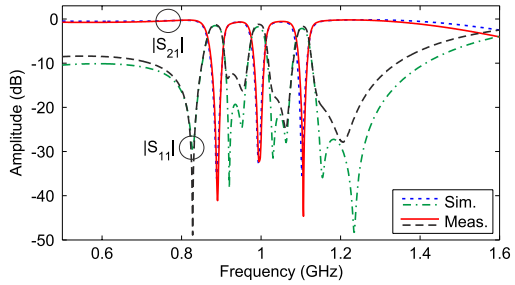

Fig. 11. Simulated and measured power transmission ($|S_{21}|$) and reflection ($|S_{11}|$) responses of the manufactured three-band second-order BSF prototype for one example state (simulation values for the capacitors as designated in Fig. 10: $C_{r1} = 5.3$ pF, $C_{r2} = 1.85$ pF, $C_{r3} = 3$ pF, $C_{c1} = 1.05$ pF, $C_{c2} = 0.75$ pF, $C_{c3} = 0.95$ pF, and estimated quality factor $Q = 150$ at 1 GHz for all the adjustable capacitors).

from Johanson Manufacturing that exhibit capacitance variation ranges of 1–5 pF and 0.5–2.5 pF were, respectively, utilized (part number: 9402-0/1SL-1)[1]—C_{r1}, C_{r2}, and C_{r3} tune the center frequencies of the first, second, and third stopbands, respectively, whereas C_{c1}, C_{c2}, and C_{c3}, as designated in Fig. 10, control their bandwidths. These mechanically adjustable capacitors exhibit a quality factor $Q > 1000$ at 100 MHz. Note also that other technologies could equally be applied for the experimental demonstration of the filtering concepts presented in this paper, for example, tunable piezoelectrically actuated capacitively loaded evanescent-mode cavity resonators as in [37] for electronically reconfigurable lower loss and higher selectivity filter implementations in 3-D volumes or MEMS-actuated resonators using high-Q capacitor arrays as tuning elements [38].

A comparison between the simulated and measured power transmission and reflection responses of the developed circuit for one specific tuned state is provided in Fig. 11. Note that the provided data for the estimated Q that is assumed to be equal for all the capacitors in the linear-circuit simulator was extracted by modifying its value until the highest matching between measurements and simulations—as shown in Fig. 11—was attained. As observed, a fairly close agreement is obtained between the simulated and experimental results. In this state, the measured power-rejection depths for the notched bands that are located at 0.89, 1, and 1.1 GHz are 41, 32, and 45 dB, respectively. The measured minimum interband power insertion-loss and input-matching levels are equal to 0.68 and 12.4 dB—between the first and second stopbands—and 0.55 and 17.5 dB—between the second and third stopbands. The reconfiguration capabilities of this filter prototype are shown in Fig. 12. In particular, Fig. 12(a) demonstrates how the eliminated bands can be independently controlled in center frequency by considering the example case of tuning the center frequency of the upper rejected band while the locations of the rest remain unchanged. In a similar manner, Fig. 12(b) shows the bandwidth control for the stopbands particularized in the lower notched band (stopband-width tuning ratio of 3.5:1 for these measured responses). It should be remarked

[1][Online]. Available: http://www.johansonmfg.com/media/pdf/ThinTrim.pdf

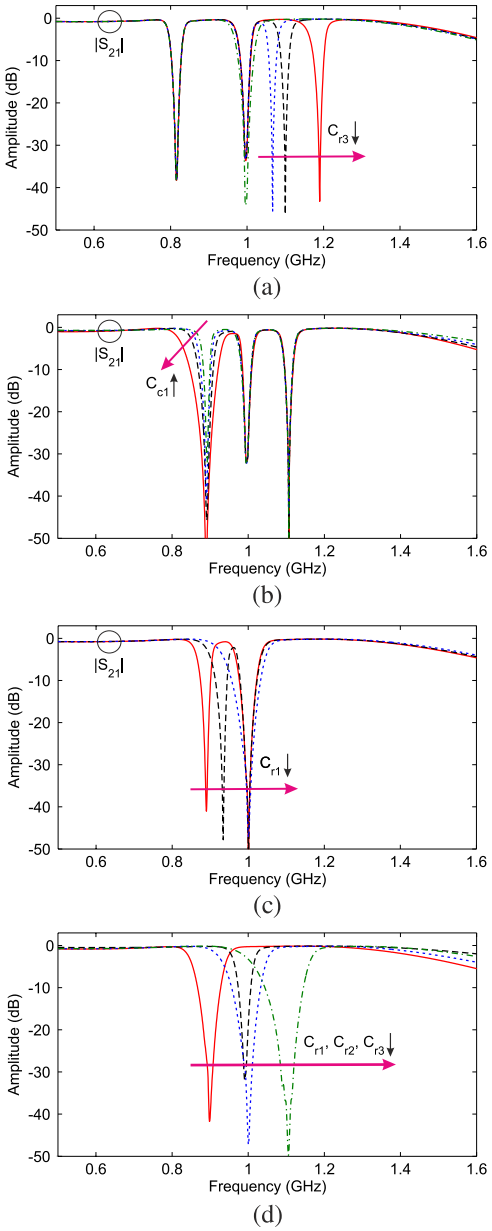

Fig. 12. Measured power transmission ($|S_{21}|$) responses of the manufactured three-band second-order BSF prototype for different reconfiguration states. (a) Center-frequency control—note that the upper eliminated band is spectrally merged with the second one in the dashed-dotted green trace. (b) Bandwidth control. (c) Center-frequency control of one rejected band when the other two are joined into a unique wider rejection band that remains static—note that the three stopbands are combined into the same suppressed band in the dotted blue trace. (d) Center-frequency and bandwidth control in a broader single-band bandstop filtering response obtained from the spectral merging of the three eliminated bands into one.

upon that the center frequencies and bandwidths of two or the three stopbands can also be varied at the same time by simultaneously tuning the variable capacitors that control them. Center-frequency tuning of the lower rejected band when the remaining ones are spectrally joined into a frequency-static and wider single stopband is validated in Fig. 12(c)—note that the three stopbands become combined into the same eliminated band in the dotted blue trace in Fig. 12(c). Furthermore, as an additional spectral-adaptivity feature of this

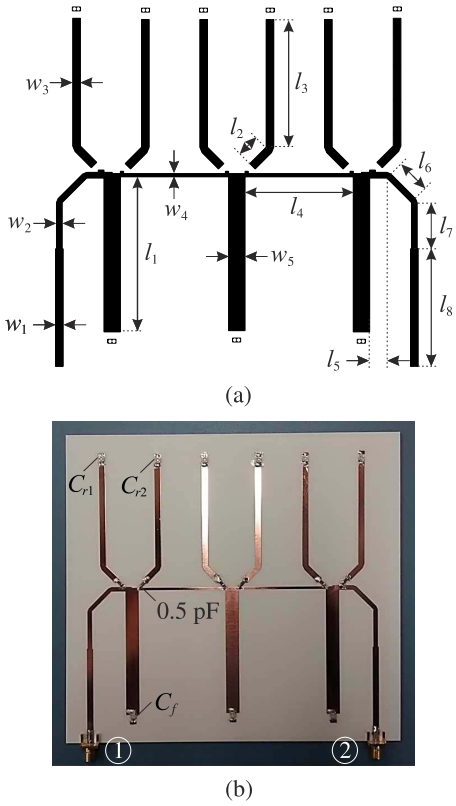

Fig. 13. Manufactured broadband BPF prototype with embedded notches. (a) Layout. Illustrated dimensions (in mm): $w_1 = 3.3$, $w_2 = 2.46$, $w_3 = 3.3$, $w_4 = 1.39$, $w_5 = 7.1$, $l_1 = 66.5$, $l_2 = 10$, $l_3 = 55.2$, $l_4 = 46.8$, $l_5 = 7.46$, $l_6 = 15$, $l_7 = 20$, and $l_8 = 50.8$. (b) Photograph.

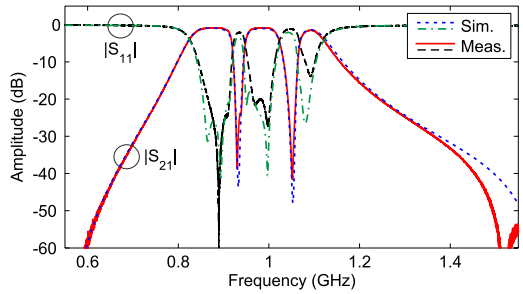

Fig. 14. Simulated and measured S-parameters—in amplitude—of the manufactured broadband BPF prototype with embedded notches for one example state (simulation values for the capacitors as designated in Fig. 16: $C_f = 3$ pF, $C_{r1} = 5$ pF, $C_{r2} = 2.5$ pF, $C_c = 0.6$ pF, and estimated quality factor $Q = 150$ at 1 GHz for all the capacitors).

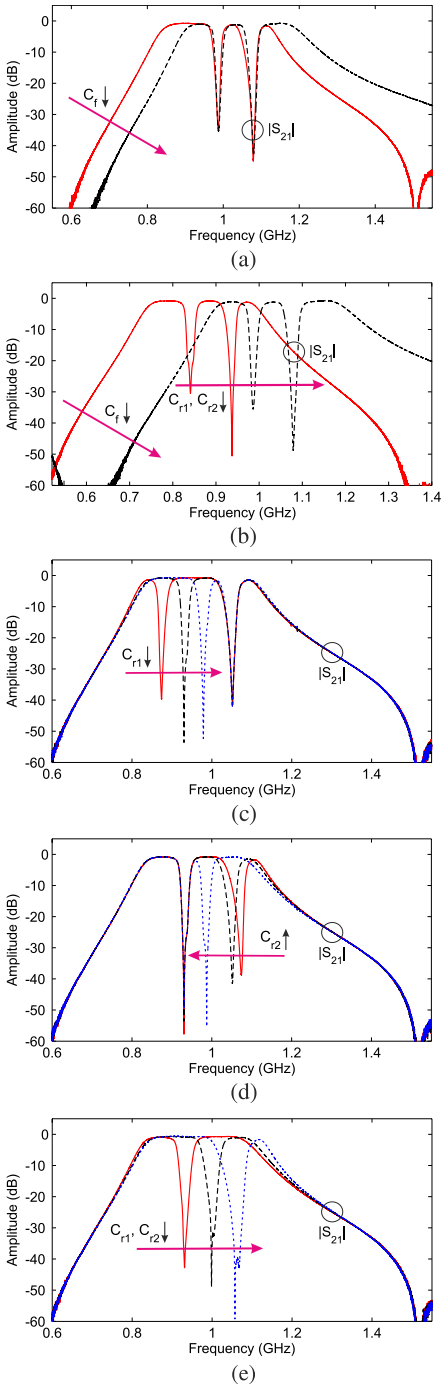

Fig. 15. Measured power transmission ($|S_{21}|$) responses of the manufactured broadband BPF prototype with embedded notches for different reconfiguration states. (a) Center-frequency control of the overall transmission passband with static notches. (b) Center-frequency control of the overall transmission passband with tuned notches. (c) Center-frequency control of the lower embedded stopband. (d) Center-frequency control of the upper embedded stopband. (e) Center-frequency control of a wider single stopband obtained from the spectral merging of the two embedded eliminated bands into one.

RF filtering prototype, Fig. 12(d) proves center-frequency and bandwidth reconfiguration of a unique second-order stopband that is shaped through the merging of the three BSF notched bands into a broader one. To the best of our knowledge, these spectral-reconfiguration properties make this tunable multiband BSF prototype as one of the most flexible devices of this type reported up to now.

B. Prototype 2

Following the RF filter concept shown in Fig. 5(a), a broadband BPF with two embedded third-order stopbands has been developed and measured as second practical example. This prototype was designed, so that both the overall passband of the wideband BPF and the inserted in-band notches can be spectrally tuned within the 0.8–1.2-GHz frequency band by means of frequency-reconfigurable resonators.

The layout and a photograph of the constructed circuit are given in Fig. 13. In this case, an RO4003 microstrip substrate

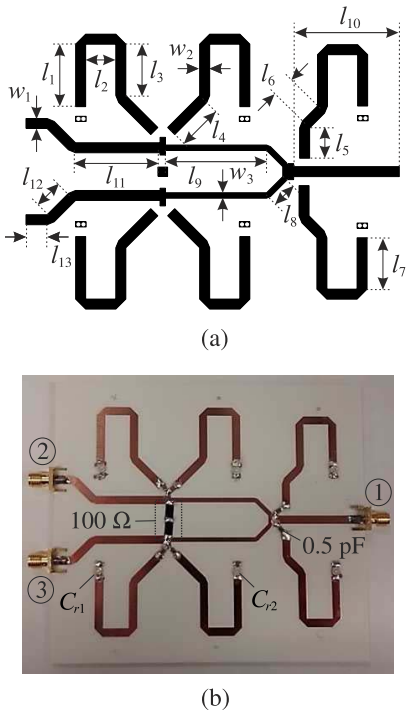

Fig. 16. Manufactured dual-notch/power-divider prototype. (a) Layout. Illustrated dimensions (in mm): $w_1 = 3.3$, $w_2 = 3.3$, $w_3 = 1.8$, $l_1 = 20.7$, $l_2 = 10$, $l_3 = 17$, $l_4 = 15$, $l_5 = 10$, $l_6 = 7$, $l_7 = 17$, $l_8 = 7.57$, $l_9 = 33.5$, $l_{10} = 35$, $l_{11} = 28$, $l_{12} = 10$, and $l_{13} = 7$. (b) Photograph.

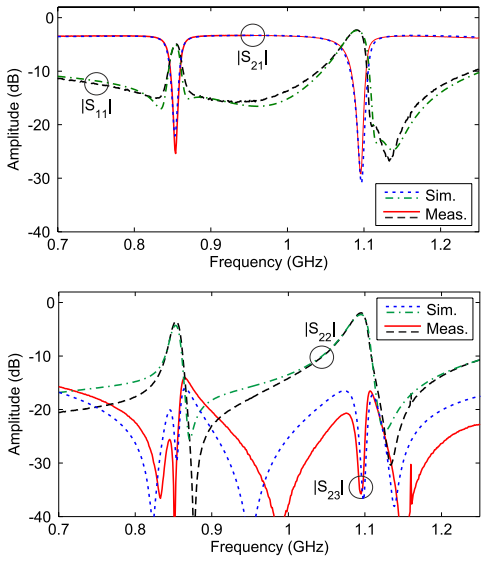

Fig. 17. Simulated and measured S-parameters—in amplitude—of the manufactured dual-notch/power-divider prototype for one example state (simulation values for the capacitors as designated in Fig. 16: $C_{r1} = 4.2$ pF, $C_{r2} = 0.6$ pF, $C_c = 0.65$ pF, and estimated quality factor $Q = 150$ at 1 GHz for all the capacitors).

with the following parameters was used for manufacturing: relative dielectric permittivity $\varepsilon_r = 3.38$, dielectric thickness $H = 1.52$ mm, metal thickness $t = 17.8$ μm, and dielectric loss tangent $\tan\delta_D = 0.0027$. The reconfigurable resonators of both the wideband BPF and the incorporated dual-notch filtering sections were implemented as uniform-impedance transmission-line segments that are loaded with ground-ended mechanically adjustable capacitors of 1–5-pF variation range (the same model as in the previous example)—C_f controls the center frequency of the overall transmission band, whereas C_{r1} and C_{r2} tune the center frequencies of the embedded lower and upper notched bands, respectively. The couplings between the resonating nodes of the dual-notch filtering sections and their adjacent NRNs were realized through 0.5-pF (±0.25-pF tolerance) static capacitors (C_c) from Samsung Microelectronics—manufacturer part number: CL31C0R5CBCNNNC (i.e., no bandwidth control is introduced in this particular circuit). The impedance inverters that connect in series the tunable resonators of the BPF were designed as quarter-wavelength transmission-line sections.

The simulated and measured power transmission and reflection responses of the built prototype for one specific tuned state are shown in Fig. 14. Again, the agreement obtained between simulated and experimental results is reasonably close. The measured minimum power insertion-loss and input-matching levels in the whole passband are 0.85 and 13.9 dB, respectively. It shows a center frequency equal to 0.97 GHz and a relative bandwidth of 30.2%. The measured power-rejection depths of the in-band notches located at 0.93 and 1.05 GHz are 38.5 and 41.5 dB, respectively. The frequency-tunability characteristics of the fabricated circuit are shown in Fig. 15. First, center-frequency control of the overall transmission band with two embedded notches is proved in Fig. 15(a) and (b)—the in-band notches remain static in Fig. 15(a), whereas they are also tuned in Fig. 15(b). The capability to tune the center frequency of the lower and upper in-band notches for one static passband is demonstrated in Fig. 15(c) and (d), respectively. Finally, the center-frequency reconfiguration of a composite third-order wider stopband shaped from the merging of the lower and upper third-order eliminated bands is exemplified in Fig. 15(e). Summarizing the aforementioned RF-measured performance metrics, the developed wideband BPF prototype with embedded notches allows a simultaneous frequency reconfiguration of its overall transmission band and in-band notches, as well as the intrinsic control, i.e., without RF switches, of the number of active rejected bands through its merging. Such spectral-adaptivity capabilities are reported in this paper for the first time for this type of dual-function RF filtering components. Furthermore, the rejection depths of the embedded notches and their tuning range are much larger than those demonstrated by related prior-art devices as the ones in [17], [18], [20], and [21].

C. Prototype 3

As the third experimental demonstrator, a 3-dB Wilkinson-type single-stage/two-way power divider with two embedded frequency-tunable second-order stopbands has been manufactured and characterized. As in the previous circuit examples, the rejected bands can be independently controlled and spectrally merged within the 0.8–1.1-GHz frequency interval.

The layout and a photograph of the constructed prototype are shown in Fig. 16. For circuit manufacturing, the same

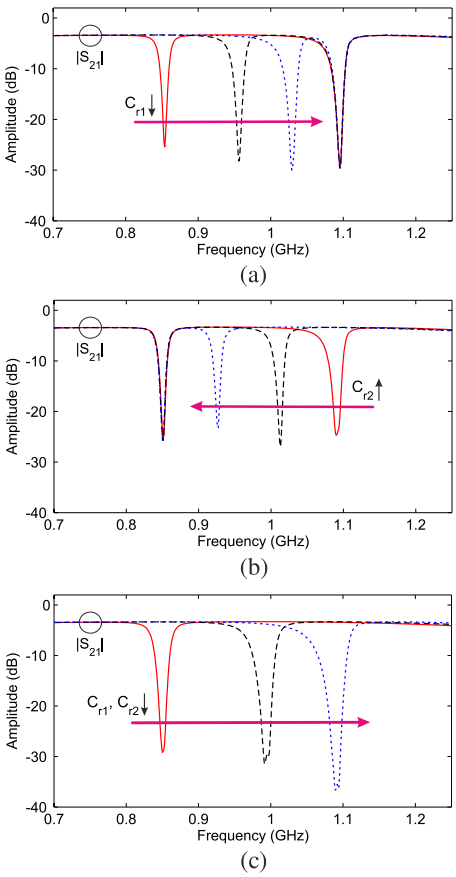

Fig. 18. Measured power transmission ($|S_{21}|$) responses of the manufactured dual-notch/power-divider prototype for different reconfiguration states. (a) Center-frequency control of the lower stopband. (b) Center-frequency control of the upper stopband. (c) Center-frequency control of a wider single stopband obtained from the spectral merging of the two eliminated bands into one.

substrate and capacitors as in the filter implementation in Section III-B were used. Furthermore, similar circuit solutions were adopted for the realization of the tunable resonators and their couplings with their contiguous NRNs—C_{r1} and C_{r2} control the center frequencies of the inserted lower and upper rejected bands, respectively. Its simulated and measured S-parameters—in amplitude—for one particular reconfigured state are compared in Fig. 17. As can be seen, measured maximum power-rejection levels of 25.5 and 29.5 dB for the notched bands centered at 0.85 and 1.1 GHz are, respectively, obtained. The measured minimum interstopband power-insertion-loss level is 3.35 dB (i.e., 0.35 dB of excess loss with regard to the 3-dB power-division factor that includes the SMA connector loss), whereas the power-isolation levels between the output terminals and the power-matching levels at all the ports are higher than 10 dB for the plotted frequency interval. The spectral-adaptivity capabilities of the developed filtering power divider are proved in Fig. 18. Independent center-frequency reconfiguration of the lower and upper suppressed bands is, respectively, verified in Fig. 18(a) and (b). Moreover, center-frequency tuning of a single and wider second-order rejected band that is obtained from the merging of the two adaptive second-order stopbands is validated in Fig. 18(c). In all these responses, comparable power-matching and power-isolation performances as in the state shown in Fig. 17 are achieved, as well as nearly identical transfer functions for both power-divider branches.

IV. Conclusion

A new type of tune-all planar multiband BSFs that feature larger number of reconfigurable transfer-function properties than related prior-art devices have been presented. The proposed RF filtering approach is based on the in-series cascade of spectrally adaptive multiband bandstop filtering cells that comprise variable resonators and adjustable impedance inverters. In this manner, an independent control of the generated stopbands in terms of center frequency and bandwidth is obtained in the overall filter architecture. Moreover, these rejected bands can be spectrally combined into wider stopbands of the same order to dynamically select the amount of active eliminated bands regardless of the number of the resonators that are used in its building multiband bandstop filtering stage. The operational principles of the engineered multiband BSF, which is practically scalable to any number of arbitrary-order stopbands, have been theoretically expounded by means of a coupling-matrix formalism. In addition, its cointegration with other RF analog-processing functionalities, such as the realization of frequency-reconfigurable wideband BPFs and Wilkinson-type power dividers with embedded multiband adaptive notches, has been investigated for the first time. Note that all these multifunctional filtering components exhibit less insertion loss and circuit size, i.e., fewer impedance inverters, when compared with their classic counterparts based on series cascades of separate monofunction RF blocks. As experimental proof-of-concept demonstrators of the devised RF filtering devices, three UHF-band mechanically reconfigurable prototypes have been manufactured in microstrip technology and measured.

References

[1] R. Gómez-García, J.-P. Magalhães, J.-M. Muñoz-Ferreras, J. M. N. Vieira, N. B. Carvalho, and J. Pawlan, "Filling the spectral holes," *IEEE Microw. Mag.*, vol. 15, no. 2, pp. 45–56, Mar./Apr. 2014.

[2] W. J. Chappell, E. J. Naglich, C. Maxey, and A. C. Guyette, "Putting the radio in 'software-defined radio': Hardware developments for adaptable RF systems," *Proc. IEEE*, vol. 102, no. 3, pp. 307–320, Mar. 2014.

[3] R. Gómez-García and A. C. Guyette, "Reconfigurable multi-band microwave filters," *IEEE Trans. Microw. Theory Techn.*, vol. 63, no. 4, pp. 1294–1307, Apr. 2015.

[4] R. Gómez-García, A. C. Guyette, D. Psychogiou, E. J. Naglich, and D. Peroulis, "Quasi-elliptic multi-band filters with center-frequency and bandwidth tunability," *IEEE Microw. Wireless Compon. Lett.*, vol. 26, no. 3, pp. 192–194, Mar. 2016.

[5] Y.-Y. Wang, F. Wei, H. Xu, B. Liu, and X.-W. Shi, "A tunable dual-stop-band filter using spurlines," in *Proc. Microw. Millim. Wave Technol. Conf.*, Shenzhen, China, May 2012, pp. 1–4.

[6] K. Lee, T. H. Lee, C. S. Ahn, Y. S. Kim, and J. Lee, "Reconfigurable dual-stopband filters with reduced number of couplings between a transmission line and resonators," *IEEE Microw. Wireless Compon. Lett.*, vol. 25, no. 2, pp. 106–108, Feb. 2015.

[7] Y.-H. Cho and G. M. Rebeiz, "Tunable 4-pole dual-notch filters for cognitive radios and carrier aggregation systems," *IEEE Trans. Microw. Theory Techn.*, vol. 63, no. 4, pp. 1308–1314, Apr. 2015.

[8] C.-H. Ko, A. Tran, and G. M. Rebeiz, "Tunable 500–1200-MHz dual-band and wide bandwidth notch filters using RF transformers," *IEEE Trans. Microw. Theory Techn.*, vol. 63, no. 6, pp. 1854–1862, Jun. 2015.

[9] D. Psychogiou, R. Gómez-García, and D. Peroulis, "High-Q bandstop filters exploiting acoustic-wave-lumped-element resonators (AWLRs)," *IEEE Trans. Circuits Syst. II, Exp. Briefs*, vol. 63, no. 1, pp. 79–83, Jan. 2016.

[10] I. C. Hunter and J. D. Rhodes, "Electronically tunable microwave bandstop filters," *IEEE Trans. Microw. Theory Techn.*, vol. MTT-30, no. 9, pp. 1361–1367, Sep. 1982.

[11] A. C. Guyette, "Alternative architectures for narrowband varactor-tuned bandpass filters," in *Proc. 39th Eur. Microw. Conf.*, Rome, Italy, Sep./Oct. 2009, pp. 1828–1831.

[12] A. Abunjaileh and I. C. Hunter, "Tunable bandpass and bandstop filters based on dual-band combline structures," *IEEE Trans. Microw. Theory Techn.*, vol. 58, no. 12, pp. 3710–3719, Dec. 2010.

[13] E. J. Naglich, J. Lee, D. Peroulis, and W. J. Chappell, "Extended pass-band bandstop filter cascade with continuous 0.85–6.6-GHz coverage," *IEEE Trans. Microw. Theory Techn.*, vol. 60, no. 1, pp. 21–30, Jan. 2012.

[14] D. Psychogiou, R. Gómez-García, and D. Peroulis, "Acoustic-wave-lumped-element-resonator filters with equi-ripple absorptive stopbands," *IEEE Microw. Wireless Compon. Lett.*, vol. 26, no. 3, pp. 177–179, Mar. 2016.

[15] F. Wei, Z. D. Wang, F. Yang, and X. W. Shi, "Compact UWB BPF with triple-notched bands based on stub loaded resonator," *Electron. Lett.*, vol. 49, no. 2, pp. 124–126, Jan. 2013.

[16] S. Kumar, R. D. Gupta, and M. S. Parihar, "Multiple band notched filter using C-shaped and E-shaped resonator for UWB applications," *IEEE Microw. Wireless Compon. Lett.*, vol. 26, no. 5, pp. 340–342, May 2016.

[17] M. Nosrati, N. Vahabisani, and M. Daneshmand, "Compact MEMS-based ultrawide-band CPW band-pass filters with single/double tunable notch-bands," *IEEE Trans. Compon., Packag., Manuf. Technol.*, vol. 4, no. 9, pp. 1451–1460, Sep. 2014.

[18] W. Feng, Y. Shang, and W. Che, "Ultra-wideband bandpass filter with reconfigurable notch bands using TCSRs," *Electron. Lett.*, vol. 51, no. 23, pp. 1893–1894, Nov. 2015.

[19] D. Psychogiou, R. Gómez-García, and D. Peroulis, "Signal-interference bandpass filters with dynamic in-band interference suppression," in *Proc. IEEE Radio Wireless Symp.*, Austin, TX, USA, Jan. 2016, pp. 80–83.

[20] R. Gómez-García and A. C. Guyette, "Two-branch channelized passive filters for lowpass and bandpass applications," in *IEEE MTT-S Int. Microw. Symp. Dig.*, San Francisco, CA, USA, May 2016, pp. 1–4.

[21] H. Wang, K.-W. Tam, S.-K. Ho, W. Kang, and W. Wu, "Design of ultra-wideband bandpass filters with fixed and reconfigurable notch bands using terminated cross-shaped resonators," *IEEE Trans. Microw. Theory Techn.*, vol. 62, no. 2, pp. 252–265, Feb. 2014.

[22] D. Psychogiou, R. Gómez-García, and D. Peroulis, "A class of fully-reconfigurable planar multi-band bandstop filters," in *IEEE MTT-S Int. Microw. Symp. Dig.*, San Francisco, CA, USA, May 2016, pp. 1–4.

[23] X. Y. Zhang, K.-X. Wang, and B.-J. Hu, "Compact filtering power divider with enhanced second-harmonic suppression," *IEEE Microw. Wireless Compon. Lett.*, vol. 23, no. 9, pp. 483–485, Sep. 2013.

[24] C.-F. Chen and C.-Y. Lin, "Compact microstrip filtering power dividers with good in-band isolation performance," *IEEE Microw. Wireless Comput. Lett.*, vol. 24, no. 1, pp. 17–19, Jan. 2014.

[25] K.-X. Wang, X. Y. Zhang, and B.-J. Hu, "Gysel power divider with arbitrary power ratios and filtering responses using coupling structure," *IEEE Trans. Microw. Theory Techn.*, vol. 63, no. 3, pp. 431–440, Mar. 2014.

[26] Y. C. Li, Q. Xue, and X. Y. Zhang, "Single- and dual-band power dividers integrated with bandpass filters," *IEEE Trans. Microw. Theory Techn.*, vol. 61, no. 1, pp. 69–76, Jan. 2013.

[27] R. Gómez-García, R. Loeches-Sánchez, D. Psychogiou, and D. Peroulis, "Single/multi-band Wilkinson-type power dividers with embedded transversal filtering sections and application to channelized filters," *IEEE Trans. Circuits Syst. I, Reg. Papers*, vol. 62, no. 6, pp. 1518–1527, Jun. 2015.

[28] C.-F. Chen, C.-Y. Lin, B.-H. Tseng, and S.-F. Chang, "Compact microstrip electronically tunable power divider with Chebyshev band-pass response," in *Proc. Asia–Pacific Microw. Conf.*, Nov. 2014, pp. 1291–1293.

[29] L. Gao, X.-Y. Zhang, and Q. Xue, "Compact tunable filtering power divider with constant absolute bandwidth," *IEEE Trans. Microw. Theory Techn.*, vol. 63, no. 10, pp. 3505–3513, Oct. 2015.

[30] P.-L. Chi and Y. Yang, "A 1.3–2.08 GHz filtering power divider with bandwidth control and high in-band isolation," *IEEE Microw. Wireless Compon. Lett.*, vol. 26, no. 6, pp. 407–409, Jun. 2016.

[31] D. Psychogiou, R. Gómez-García, A. C. Guyette, and D. Peroulis, "Reconfigurable single-/multi-band filtering power divider based on quasi-bandpass sections," *IEEE Microw. Wireless Compon. Lett.*, vol. 26, no. 3, pp. 684–686, Sep. 2016.

[32] J.-S. Hong, *Microstrip Filters for RF/Microwave Applications*, 2nd ed. Piscataway, NJ, USA: IEEE Press, 2011.

[33] A. Garcia-Lamperez and M. Salazar-Palma, "Single-band to multiband frequency transformation for multiband filters," *IEEE Trans. Microw. Theory Techn.*, vol. 59, no. 11, pp. 3048–3058, Dec. 2011.

[34] S. B. Cohn, "A class of broadband three-port TEM-mode hybrids," *IEEE Trans. Microw. Theory Techn.*, vol. MTT-16, no. 2, pp. 110–116, Feb. 1968.

[35] E. J. Naglich and A. C. Guyette, "Reflection-mode bandstop filters with minimum through-line length," *IEEE Trans. Microw. Theory Techn.*, vol. 63, no. 10, pp. 3479–3486, Oct. 2015.

[36] A. C. Guyette and E. J. Naglich, "Short-through-line bandstop filters using dual-coupled resonators," *IEEE Trans. Microw. Theory Techn.*, vol. 64, no. 2, pp. 459–466, Feb. 2016.

[37] D. Psychogiou, R. Gómez-García, and D. Peroulis, "Fully-reconfigurable bandpass/bandstop filters and their coupling-matrix representation," *IEEE Microw. Wireless Compon. Lett.*, vol. 26, no. 1, pp. 22–24, Jan. 2016.

[38] M. D. Hickle, J. Li, D. Psychogiou, and D. Peroulis, "A high-performance pathway: A 0.95/2.45-GHz switched-frequency bandpass filter using commercially available RF MEMS tuning elements," *IEEE Microw. Mag.*, vol. 17, no. 3, pp. 34–41, Mar. 2016.

Dimitra Psychogiou (S'10–M'14) received the Dipl.Eng. degree in electrical and computer engineering from the University of Patras, Patras, Greece, in 2008, and the Ph.D. degree in electrical engineering from the Swiss Federal Institute of Technology, ETH Zürich, Zürich, Switzerland, in 2013.

In 2008, she joined the Wireless Communication Research Group, University of Loughborough, Loughborough, U.K., as a Research Assistant. From 2013 to 2016, she was with Purdue University, West Lafayette, IN, USA. Since 2016, she has been with the Department of Electrical, Computer, and Energy Engineering, University of Colorado at Boulder, Boulder, CO, USA, as an Assistant Professor. Her current research interests include RF design and characterization of reconfigurable microwave and millimeter-wave passive components and RF circuits, RF microelectromechanical systems, acoustic-wave resonator-based filters, tunable filter synthesis, and frequency-agile antennas.

Dr. Psychogiou is an Associate Editor of IET's *Microwaves, Antennas, and Propagation*.

Roberto Gómez-García (S'02–M'06–SM'11) was born in Madrid, Spain, in 1977. He received the degree in telecommunication engineering and the Ph.D. degree in electrical and electronic engineering from the Polytechnic University of Madrid, Madrid, in 2001 and 2006, respectively.

Since 2006, he has been an Associate Professor with the Department of Signal Theory and Communications, University of Alcalá, Alcalá de Henares, Madrid. He has been, for several research stays, with the C2S2 Department, XLIM Research Institute, University of Limoges, Limoges, France, the Telecommunications Institute, University of Aveiro, Aveiro, Portugal, the U.S. Naval Research Laboratory, Microwave Technology Branch, Washington, DC, USA, and Purdue University, West Lafayette, IN, USA. His current research interests include the design of fixed/tunable high-frequency filters and multiplexers in planar, hybrid, and monolithic microwave-integrated circuit technologies, multifunction circuits and systems, and software-defined radio and radar architectures for telecommunications, remote sensing, and biomedical applications.

Dr. Gómez-García was the recipient of the 2016 IEEE Microwave Theory and Techniques Society (MTT-S) Outstanding Young Engineer Award. From 2012 to 2015, he was an Associate Editor of the IEEE TRANSACTIONS ON CIRCUITS AND SYSTEMS—I: REGULAR PAPERS. He was a Guest Editor of the 2013 IEEE JOURNAL ON EMERGING AND SELECTED TOPICS IN CIRCUITS AND SYSTEMS "Special Issue on Advanced Circuits and Systems for CR/SDR Applications," the *IET Microwaves, Antennas, and Propagation* 2013 "Special Issue on Advanced Tunable/Reconfigurable and Multi-Function RF/Microwave Filtering Devices," and the *IEEE Microwave Magazine* 2014 "Special Issue on Recent Trends on RF/Microwave Tunable Filter Design." He is currently an Associate Editor of the IEEE TRANSACTIONS OF MICROWAVE THEORY AND TECHNIQUES and the *IET Microwaves, Antennas, and Propagation*, and a Senior Editor of the IEEE JOURNAL ON EMERGING AND SELECTED TOPICS IN CIRCUITS AND SYSTEMS. He is also a Reviewer for several IEEE, IET, EuMA, and Wiley journals. He serves as a member of the Technical Review Board for several IEEE and EuMA conferences. He is also a member of the IEEE MTT-S Filters and Passive Components (MTT-8), the IEEE MTT-S Biological Effect and Medical Applications of RF and Microwave (MTT-10), the IEEE MTT-S Wireless Communications (MTT-20), and the IEEE CAS-S Analog Signal Processing Technical Committees.

Dimitrios Peroulis (S'99–M'04–SM'15) received the Ph.D. degree in electrical engineering from the University of Michigan at Ann Arbor, Ann Arbor, MI, USA, in 2003.

He has been with Purdue University, West Lafayette, IN, USA, since 2003, where he is currently a Professor of electrical engineering and the Deputy Director of the Birck Nanotechnology Center. He has been a Key Contributor on developing very high-quality ($Q > 1000$) RF microelectromechanical systems (MEMS) tunable filters (1–100 GHz) in mobile form factors. He has been investigating failure modes of RF MEMS and MEMS sensors through the DARPA M/NEMS S&T Fundamentals Program (Phases I and II) and the Center for the Prediction of Reliability, Integrity, and Survivability of Microsystems funded by the National Nuclear Security Administration. He has co-authored over 300 journal and conference papers. His current research interests include reconfigurable electronics, RF MEMS, and sensors in harsh environment applications.

Dr. Peroulis was the recipient of the National Science Foundation CAREER Award in 2008, the Outstanding Paper Award from the IEEE Ultrasonics, Ferroelectrics, and Frequency Control Society (Ferroelectrics Section) in 2012, and the Outstanding Young Engineer Award of the IEEE Microwave Theory and Techniques Society (MTT-S) in 2014. His students have been the recipients of numerous Student Paper Awards and other student research-based scholarships. He is a Purdue University Faculty Scholar. He has also been the recipient of ten teaching awards, including the 2010 HKN C. Holmes MacDonald Outstanding Teaching Award and the 2010 Charles B. Murphy Award, which is Purdue University's highest undergraduate teaching honor.